International Journal of Neural Systems (2021) 2150010 (18 pages)

DOI: 10.1142/S0129065721500106

Concurrent Prediction of Finger Forces Based on Source Separation and Classification of Neuron Discharge Information

Yang Zheng* and Xiaogang Hu†
Joint Department of Biomedical Engineering
University of North Carolina — Chapel Hill
and North Carolina State University
Raleigh, NC, USA
**yang1127@email.unc.edu*
†xiaogang@unc.edu

Received 9 December 2020
Accepted 10 December 2020
Published Online

A reliable neural-machine interface is essential for humans to intuitively interact with advanced robotic hands in an unconstrained environment. Existing neural decoding approaches utilize either discrete hand gesture-based pattern recognition or continuous force decoding with one finger at a time. We developed a neural decoding technique that allowed continuous and concurrent prediction of forces of different fingers based on spinal motoneuron firing information. High-density skin-surface electromyogram (HD-EMG) signals of finger extensor muscle were recorded, while human participants produced isometric flexion forces in a dexterous manner (i.e. produced varying forces using either a single finger or multiple fingers concurrently). Motoneuron firing information was extracted from the EMG signals using a blind source separation technique, and each identified neuron was further classified to be associated with a given finger. The forces of individual fingers were then predicted concurrently by utilizing the corresponding motoneuron pool firing frequency of individual fingers. Compared with conventional approaches, our technique led to better prediction performances, i.e. a higher correlation (0.71 ± 0.11 versus 0.61 ± 0.09), a lower prediction error ($5.88 \pm 1.34\%$ MVC versus $7.56 \pm 1.60\%$ MVC), and a higher accuracy in finger state (rest/active) prediction ($88.10 \pm 4.65\%$ versus $80.21 \pm 4.32\%$). Our decoding method demonstrated the possibility of classifying motoneurons for different fingers, which significantly alleviated the cross-talk issue of EMG recordings from neighboring hand muscles, and allowed the decoding of finger forces individually and concurrently. The outcomes offered a robust neural-machine interface that could allow users to intuitively control robotic hands in a dexterous manner.

Keywords: Neurosignal processing; finger force prediction; hand function; motor unit; neural interface.

1. Introduction

Manual dexterity allows humans to use our hands in a skillful and coordinated way to produce a variety of precisely controlled movements. With exciting development of robotics, advanced prosthetic and exoskeletal hands now have the ability to control individual fingers or even individual joints,[1] and the dexterity is approaching the human hand. To make full use of these advanced robots for rehabilitation, assistance, or remote operation purposes, a reliable neural-machine interface is essential for seamless human–robot interactions. Neural signals can be obtained at different levels including brain,[2–4] peripheral nerve,[5,6] and muscles.[7–9] These signals are processed to identify the user's intention and are

†Corresponding author.

translated into commands to interface with external devices, termed movement decoding.[10–12] Biomechanical measurements of body segments have also been used to either predict intent[13,14] or therapeutic outcomes.[15–17] Currently, the decoding of individual finger movements remains a substantial challenge in neural-machine interface. Finger kinematics can be predicted from electrocorticogram or intracortical recordings on the motor cortex.[18,19] Motoneuron discharge information obtained directly at the peripheral nerve through nerve implants has also been used to predict finger kinematics.[5,20] Despite the success, the low signal quality and invasive nature of these methods limit wide applications.

Surface electromyography (sEMG) is a noninvasive approach to obtain muscle activities from the skin surface,[21] which constitutes the temporal and spatial summation of hundreds of motor unit action potentials (MUAP) from motoneuron discharge events of active motor units (MUs) (Fig. 1). Decoding of movement intention from sEMG has been widely used in neural-machine interface due to its noninvasive nature.[22–24] Current state-of-the-art decoding methods use pattern recognition techniques,[25,26] which recognize specific patterns of muscle activity and translate them into a set of predefined commands, such as hand open or close. Even though a large number of hand motions can be classified,[26] the motions cannot be identified in a continuous manner. A second approach, termed proportional control,[22,27] enables users to control a single degree of freedom (DOF) in a continuous manner by varying the control input such as the EMG amplitude. Intuitively, by placing the electrodes at different muscles or muscle compartments, the muscle activity associated with the movements of different fingers could be acquired via different electrodes. The information can then be converted into control inputs for different degrees of freedom of the robots. However, since individual finger muscles or muscle compartments are anatomically close to each other, a single electrode can inevitably capture

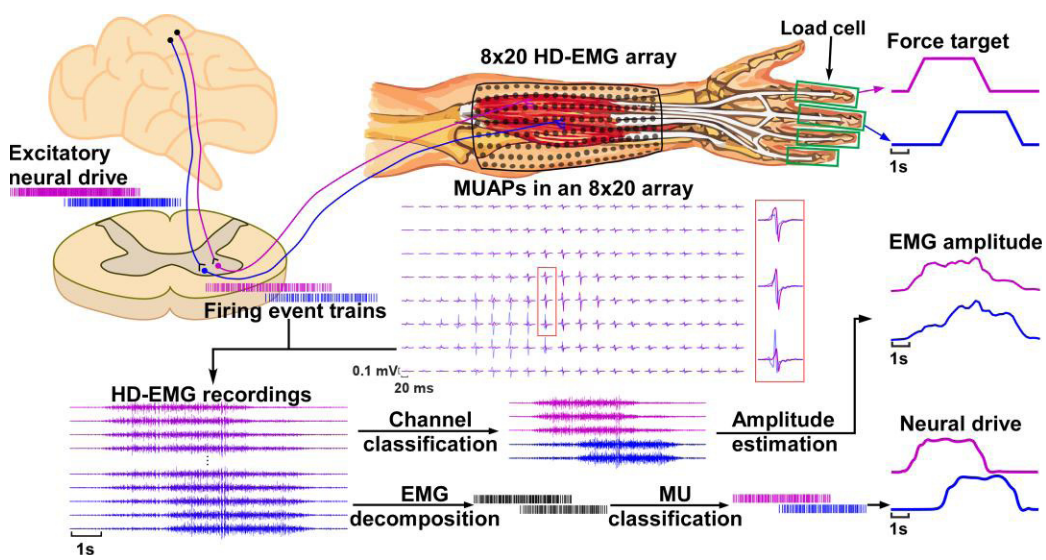

Fig. 1. (Color online) High-density electromyogram (EMG) recordings, and the force prediction procedures using the conventional EMG amplitude-based method and the neural-drive method. Two groups of motoneurons (blue and purple) innervate different finger muscles. A motoneuron discharge can generate motor unit action potentials (MUAPs) recorded at different locations of the skin surface (MUAPs in an 8×20 recording array). EMG recordings reflect the temporal and spatial summation of different MUAPs of all activated motor units (MUs). In the conventional EMG amplitude-based method, an EMG channel selection procedure is conducted, and the EMG channels are classified into different groups that reflect the muscle activities of different fingers. EMG amplitude can then predict the forces of individual fingers. In the neural-drive method, MU firing activities are first extracted through EMG decomposition (source separation and clustering). A MU classification is then used to categorize the MUs into different groups for different fingers. The neural drive is calculated as the populational firing frequency of the MU pool to predict the forces of individual fingers.

activities from nearby muscles or muscle compartments of different fingers.[28,29] Additionally, multiple intrinsic and extrinsic interference can substantially bias EMG recordings, such as cancellation of superimposed MUAPs, background noise, motion artifact, and muscle fatigue.[30,31] All these factors can impose a challenge to decode individual finger movements when global EMG features are used,[32,33] such as Mean Absolute Value, Root Mean Square (RMS), Zero Crossing, and Slope Sign Changes.[34]

Instead of using global EMG features, MU discharge information (firing event trains in Fig. 1) can be employed to predict the motor output.[35] because the discharge frequency of the MUs at the population level reflects the descending neural drive (i.e. net excitatory drive) input to the spinal cord, which transforms the neural drive to the motoneurons into MU firing event trains.[36] It has been demonstrated that the neural drive information (decoded from the binary events of neuronal firings) is more robust for motor output decoding compared with global EMG features, during isometric muscle contractions,[37,38] and joint movements.[39,40] This is largely because the neural drive information is less sensitive to intrinsic and extrinsic interference to EMG signals. These studies predicted forces one finger at a time. However, there are partially overlapping muscle compartments of different fingers and co-activation of these compartments. It remains a substantial challenge to concurrently decode the neural drive to individual fingers in a continuous manner when the finger (thumb excluded) forces vary randomly (i.e. produced varying forces using either a single finger or multiple fingers concurrently). Accordingly, the current study sought to develop a neural decoding method based on firing frequency summed across MUs (termed neural-drive method), in order to predict the extension forces of individual fingers concurrently and continuously (Fig. 1). The conventional EMG amplitude-based force prediction method was also performed as a comparison.

This paper was organized as follows. Section 2 describes the experiment procedures and methodologies in the proposed neural-drive method and the conventional EMG amplitude-based method. Section 3 evaluates the performance of the proposed method in comparison with the conventional method. The discussion and conclusion were drawn in Sec. 4.

2. Methods

2.1. *Experimental design*

Eight subjects (one female, seven males, age: 21–35) without any known neural or muscular disorders were recruited in this study. All subjects gave informed consent with protocols approved by the Institutional Review Board of the University of North Carolina at Chapel Hill (Approval #: 16-0801).

The subjects were seated comfortably in a height-adjustable chair during the experiment. The forearm was supported on the desk at the neutral position with a soft foam. The palm and back sides of the hand was restricted to avoid force contaminations. The index, middle, ring, and pinky fingers were individually secured to four miniature load cells (SM-200N, Interface), to measure individual finger extension forces (Fig. 1). The subjects were asked to perform isometric finger extensions at various force levels using one or multiple fingers. Earlier studies have reported a relatively large enslaving effect between the ring and pinky fingers,[41,42] compared with other finger pairs. The activation patterns of the extensor digitorum communis (EDC) muscle compartments of the ring and pinky fingers were also similar based on surface EMG recordings.[43] As a result, these two fingers were always requested to extend concurrently and their forces were summed-up before displayed to the subjects and during post-processing.

Before the main experiment, the maximum voluntary contraction (MVC) forces of individual fingers were measured when the subjects performed maximum isometric extension of individual fingers. During the experiment, two different types of tasks were performed. The first type (termed *single-finger task*) involved single finger (ring and pinky were considered as one finger) extension that followed a trapezoid force target with the maximum contraction level at 50% MVC, with a trial duration of 21 s. Subjects were instructed to minimize co-activation of other fingers. In the second type (termed *multi-finger task*), the target force contained a series of trapezoids with 1-s rest in between for a duration of 36 (three fingers involved) or 12 (two fingers involved) s, and the maximum contraction level was 50% MVC. Subjects were requested to extend at least two different fingers, which were selected randomly before each trial. Co-contraction of other fingers was allowed in the multi-finger trials. Fifteen single-finger trials were performed with five trials for each finger and 28 multi-finger trials were also performed.

The force data were sampled at 1000 Hz and displayed to the subjects. An 8×20 high-density (HD) electrode array with a 3-mm single electrode diameter and a 10-mm inter-electrode distance was placed over the EDC muscles. The placement of the array was guided by palpating the EDC muscle when the subjects extended their fingers. Monopolar EMG signals were amplified with a gain of 1000 and a pass band of 10–900 Hz and were sampled at 2048 Hz via EMG-USB2+ (OT Bioelettronica).

2.2. *Force prediction using MU discharge information*

The processing included two main steps: MU extraction and MU pool refinement for individual fingers. The data in the single-finger trials were first used to extract the MU information. The multi-finger trials were randomly divided into four sets evenly, with seven trials in each set to perform a four-fold cross-evaluation. For each fold of evaluation, a single set was selected as the testing set and the remaining three were the training sets. The force prediction performance was assessed using the multi-finger trials in the testing set, and the trials in the training sets were used for the MU pool (Sec. 2.2.2) refinement procedure, in order to avoid in-sample optimization bias.

2.2.1. *Extraction of MU information*

The EMG decomposition procedure[44–46] was implemented to extract the firing information of individual MUs through the FastICA algorithm,[47] which has been used in previous studies on EMG decomposition.[48–50] Specifically, given an $m \times D$ matrix $\mathbf{X}$ representing the original HD skin-surface electromyogram (HD-EMG) recordings, where m is the number of EMG channels and D is the duration of the recordings (in sample points). The procedure to extract the information of individual MUs is as follows:

(1) Extend the raw EMG signals by adding R ($R = 10$) delayed versions of each observation, obtaining the new data matrix $\underline{\mathbf{X}}$ with a dimension of $m(R+1) \times D$.
(2) Whiten the extended signals $\mathbf{Z} = \mathbf{W}\underline{\mathbf{X}}$ with the whitening matrix $\mathbf{W}$ obtained via eigenvalue decomposition.
(3) Decompose the signals using the FastICA algorithm[47]:
   (a) Select the skewness $G(x) = x^3/3$ as the contrast function for fast convergence, which has been used in our previous study.[37]
   (b) Start the iteration procedure and the iteration is considered converged if the old ($\mathbf{w}(n)$) and new ($\mathbf{w}(n+1)$) separation vectors point to the same direction, i.e. $|\mathbf{w}(n)\mathbf{w}(n+1)^T - 1| < \mathit{threshold}$, where n is the number of iterations and *threshold* equals 10^{-4} in this study.
   (c) Repeat the iteration procedure multiple times (300 here) and obtain the separation vectors $\mathbf{w}_i (i = 1, 2, \ldots, 300)$ of 300 'MUs', which constitute the separation matrix $\mathbf{B}_0 = [\mathbf{w}_1, \mathbf{w}_2, \ldots, \mathbf{w}_{300}]$.
   (d) Get the source signal $\mathbf{s}$ for individual MUs by Eq. (1).

$$\mathbf{s}_i = \mathbf{w}_i^{\mathrm{T}}\mathbf{Z} \quad i = 1, 2, \ldots, 300. \tag{1}$$

(4) Convert the source signal to a binary firing event train, $\mathbf{t}_i$, $i = 1, 2, \ldots, 300$. All peaks in $\mathbf{s}$ are identified and classified into two categories through a binary cluster classification using the *K-means++* algorithm.[51] Peaks in the category with large values are considered the timing of firing events, and are set to 1. Other peaks and nonpeak samples are set to 0.
(5) Remove the separation vectors corresponding to the source signals with poor classification quality using the silhouette distance, resulting in n_1 separation vectors $\mathbf{B}_1 = [\mathbf{w}_1, \mathbf{w}_2, \ldots, \mathbf{w}_{n_1}]$.

   The silhouette value for the ith peak, S_i, is defined as follows:

$$S_i = \frac{b_i - a_i}{\max(a_i, b_i)}, \tag{2}$$

where a_i is the average Euclidean distance from the ith peak to the other peaks in the same cluster as i, and b_i is the minimum average Euclidean distance from the ith peak to points in a different cluster. The silhouette value ranges from -1 to $+1$. A high silhouette value indicates that the peak is well-matched to its own cluster. The overall binary classification quality was then calculated as a weighted average of the silhouette distance of each cluster (termed SIL):

$$\mathrm{SIL} = \left(\frac{1}{C_1} \sum_{i=1}^{C_1} S_i^1 + \frac{1}{C_2} \sum_{j=1}^{C_2} S_j^2 \right) \Bigg/ 2, \quad (3)$$

where S_i^1 is the silhouette value for the ith peak in cluster 1, S_j^2 is the silhouette value for the jth peak in cluster 2, C_1 and C_2 are the number of peaks in clusters 1 and 2, respectively. A source signal with a low SIL value meant that the spikes were not well separated from the baseline noise, and the detected firing events could be inaccurate. Therefore, the MUs corresponding to source signals with low SIL values (<0.7) were excluded from further analysis. The selection of the SIL threshold was mainly based on our preliminary test to guarantee the accuracy of the firing events while maintaining enough MUs for the neural-drive estimation.

(6) Remove the separation vectors of duplicate MUs, resulting in n_2 separation vectors $\mathbf{B}_2 = [\mathbf{w}_1, \mathbf{w}_2, \ldots, \mathbf{w}_{n_2}]$.

Due to the extension procedure in Step 1, different source signals might reflect the activity of the same MU. Based on the extension factor and the sampling rate, a ± 2.5 ms ($10/2048 * 1000$ ms ≈ 5 ms) window was used to quantify the synchronization level between two firing event trains. If any of the two firing event trains had more than 80% synchronized discharge events after shifting the delay within ± 2.5 ms, the two firing event trains were considered to be duplicates and the one with a smaller SIL value was excluded from further analysis.

The extraction of MU information was implemented using the single-finger trials. After the removal of duplicate MUs and MUs with low SIL values, all the MUs of the same target finger were pooled together to constitute the MU pool for individual fingers, resulting in three separation matrixes, i.e. $\mathbf{B}_{2,\mathrm{I}}$, $\mathbf{B}_{2,\mathrm{M}}$, and $\mathbf{B}_{2,\mathrm{RP}}$ for the index (I), middle (M), and ring-pinky (RP) fingers, respectively. This can be considered as a *preliminary* classification of MUs into different fingers. To maintain this classification of MUs, the separation vectors from the single-finger trials were applied directly to the EMG recordings (after extension and whitening) of the multi-finger trials for force prediction. This method has been used in a previous study[37] to obtain the firing event trains of the given MUs in *real-time* decoding.

Figure 2(a) illustrates the recorded forces of a representative single-finger trial with the index finger as the target finger. The MU firing event trains are shown in Fig. 2(b). The blue curve represents the normalized populational discharge frequency of all the MUs, which reflects the neural drive. However, the neural drive signal increased substantially even though the actual force level plateaued. This inconsistency meant that the MU pool at this stage for a specific finger possibly included some MUs of other fingers due to muscle compartment co-contractions, which led to the overestimation of neural drive signals for the specific finger.

2.2.2. *MU pool refinement for individual fingers*

To reduce the interference of co-contractions, an MU pool refinement procedure was performed to remove the MUs of other fingers using the multi-finger trials in the training set. For example, to remove the separation vectors of MUs associated with the middle and RP fingers from the separation matrix $\mathbf{B}_{2,\mathrm{I}}$, the following procedures were performed. The rational was that the firing rate of the MUs of a given finger should be correlated with the force of that specific finger.

(1) Apply the separation vectors to the EMG signals of the multi-finger trials to obtain the source signals $\mathbf{s}_{i,\mathrm{I}}$ ($i = 1, 2, \ldots, n_{2,\mathrm{I}}$) using Eq. (1). $n_{2,\mathrm{I}}$ is the number of separation vectors in matrix $\mathbf{B}_{2,\mathrm{I}}$.
(2) Convert $\mathbf{s}_{i,\mathrm{I}}$ to firing event trains $\mathbf{t}_{i,\mathrm{I}}$ and calculate the SIL values of individual trains. The firing event trains are eliminated if the SIL values are <0.6 (Fig. 2(d)).
(3) Calculate the time courses of the firing rate ($\mathbf{f}_{i,\mathrm{I}}$) of individual MUs (Fig. 2(d)). The firing event train of each MU is segmented using 0.5-s sliding windows with a sliding step of 0.1 s, and the firing rate from each 0.5-s window is calculated (if not specified, the sliding windows are the same in subsequent text).
(4) Process the forces of the three fingers using the same sliding window, obtaining the forces of individual fingers $\mathbf{F}_l^{\mathrm{trn}} (l = \mathrm{I}, \mathrm{M}, \mathrm{RP})$.
(5) Perform a linear regression analysis between the firing rate ($\mathbf{f}_{i,\mathrm{I}}$) and the forces of individual fingers $\mathbf{F}_l^{\mathrm{trn}}$. For example, obtain the coefficient of determination $R^2_{i,\mathrm{I}-l}$ between the ith MU of the

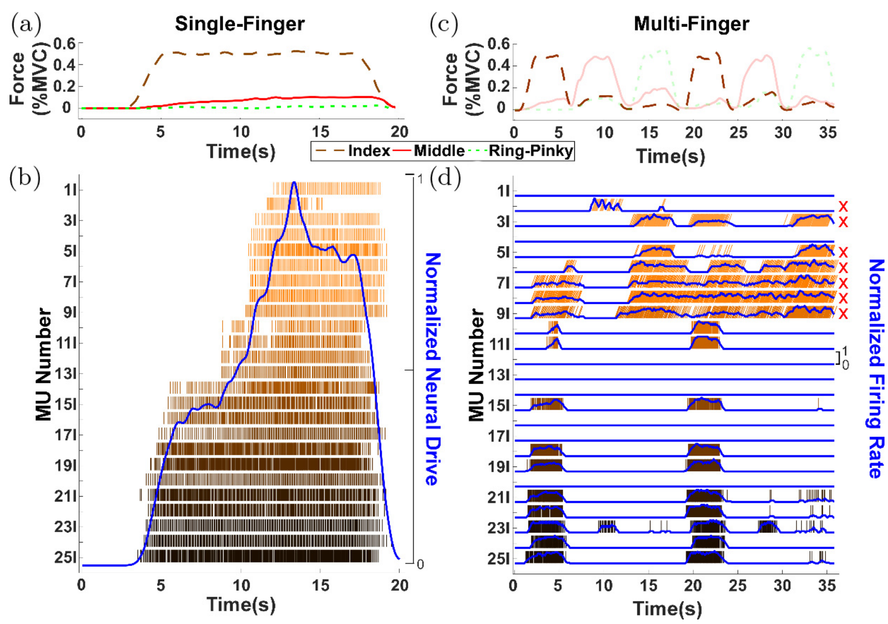

Fig. 2. (Color online) Extraction of motor unit (MU) information through electromyogram (EMG) decomposition, and refinement of the MU pool for the exemplar index finger in the neural-drive method. (a) The recorded forces of a representative single-finger trial are shown. (b) The firing event trains of individual MUs as vertical bars are obtained through EMG decomposition of the single-finger trial corresponding to the finger forces shown in (a). The blue curve represents the populational discharge frequency of all MUs, which is proportional to the neural drive. (c) The finger forces of a representative multi-finger trial. The force data of the middle and ring-pinky (RP) fingers are in shaded color to give a better illustration of the force of the index finger. (d) The MU firing event trains are obtained by applying the separation vectors of MUs obtained from the single-finger trial shown in (b) to the multi-finger trial. The blue curves represent the time courses of the normalized firing rates of individual MUs. The MUs with italic bars and red crosses (e.g. MU2I-3I and MU5I-9I) are excluded from the MU pool of the index finger because their firing rates have a weaker correlation with the force of the index finger compared with other fingers. The MUs with vertical bars are retained for the index finger.

index (I) finger and the force of finger l. All the multi-finger trials in the training set were used to refine the MU pool and the $R^2_{i,\mathrm{I}-l}$ values were averaged across all trials.

(6) Remove the separation vector of the MUs of a given finger with lower coefficients. Take index finger as an example, if $R^2_{i,\mathrm{I-I}} < R^2_{i,\mathrm{I-M}}$ or $R^2_{i,\mathrm{I-I}} < R^2_{i,\mathrm{I-PR}}$ (Fig. 2(d)), ith MU of the index (I) finger is removed. To this end, the refined MU pools specific to individual fingers, i.e. $\mathbf{B}_{3,\mathrm{I}}$, $\mathbf{B}_{3,\mathrm{M}}$, and $\mathbf{B}_{3,\mathrm{RP}}$ were obtained to predict the force of individual fingers.

In Step (2), a lower threshold was selected here because the separation vectors were obtained using the single-finger trials, and their performance would typically decrease due to variations of EMG activity in the multi-finger trials compared with the single-finger trial. The firing event train would have a SIL value lower than the threshold typically when the corresponding MUs were de-recruited (e.g. MU 1I, 4I, 12I–14I, 16I, 17I, and 20I in Fig. 2(d)).

2.2.3. *Force prediction using neural drive signals*

For a given multi-finger trial in the testing set, the force prediction performance was evaluated via the following procedure:

(1) Apply the separation vectors of individual fingers to the EMG signals to obtain the source signals $\mathbf{s}_{i,\mathrm{I}}(i = 1, 2, \ldots, n_{3,\mathrm{I}})$, $\mathbf{s}_{j,\mathrm{M}}(j = 1, 2, \ldots, n_{3,\mathrm{M}})$, and $\mathbf{s}_{k,\mathrm{RP}}(k = 1, 2, \ldots, n_{3,\mathrm{RP}})$, where $n_{3,\mathrm{I}}$, $n_{3,\mathrm{M}}$, and $n_{3,\mathrm{RP}}$ are the number of MUs after MU pool refinement for the index, middle, and RP fingers, respectively.
(2) Convert $\mathbf{s}_{i,\mathrm{I}}$, $\mathbf{s}_{j,\mathrm{M}}$, and $\mathbf{s}_{k,\mathrm{RP}}$ to the firing event trains $\mathbf{t}_{i,\mathrm{I}}$, $\mathbf{t}_{j,\mathrm{M}}$, and $\mathbf{t}_{k,\mathrm{RP}}$, and calculate the SIL

values of individual trains. The firing events were eliminated if the SIL values were smaller than 0.6.

(3) Calculate the time courses of firing rate ($\mathbf{f}_{i,\mathrm{I}}$, $\mathbf{f}_{j,\mathrm{M}}$, and $\mathbf{f}_{k,\mathrm{RP}}$) for individual MUs using the sliding window.

(4) Calculate the neural drive signals for individual fingers as

$$\mathbf{D}_l = \sum_i \mathbf{f}_{i,l} \quad l = \mathrm{I}, \mathrm{M}, \mathrm{RP}. \tag{4}$$

(5) Smoothen the neural drive signal using a Kalman filter with the system matrix, the observation matrix, the system covariance and the observation covariance set to 1, 1, 0.1, and 0.5, respectively, in order to eliminate sporadic, isolated, and large-amplitude fluctuations.[37,52] (if not specified, the Kalman filter settings are the same in the subsequent text).

(6) Process the force of individual fingers using the average window, resulting in $\mathbf{F}_l^{\mathrm{tst}}(l = \mathrm{I}, \mathrm{M}, \mathrm{RP})$.

(7) Use a linear regression model to establish the relation between the neural drive signal and the force of the corresponding finger.

$$\mathbf{F}_l^{\mathrm{tst}} = a_l \mathbf{D}_l + b_l \quad l = \mathrm{I}, \mathrm{M}, \mathrm{RP}. \tag{5}$$

(8) Use the resultant R^2 value and the root mean square error (RMSE) between the predicted force and the actual force to quantify the force prediction performance.

2.3. *Force prediction using EMG amplitude information*

The finger extension force was also predicted using the EMG amplitude information as a comparison. Earlier work has shown that the EMG amplitude was a preferred feature for force prediction among the different time and frequency features.[53] Two different EMG amplitude-based methods were performed in this study. In the first method, the number of EMG channels to calculate muscle activation strength was fixed to 60 for different fingers (termed the EMG60-amp method). The specific procedures are described as follows:

(1) Calculate the EMG amplitude (RMS) for individual channels using the single-finger trials (Fig. 3(b)).

(2) Average the amplitude across the single-finger trials with the same target finger respectively for individual channels.

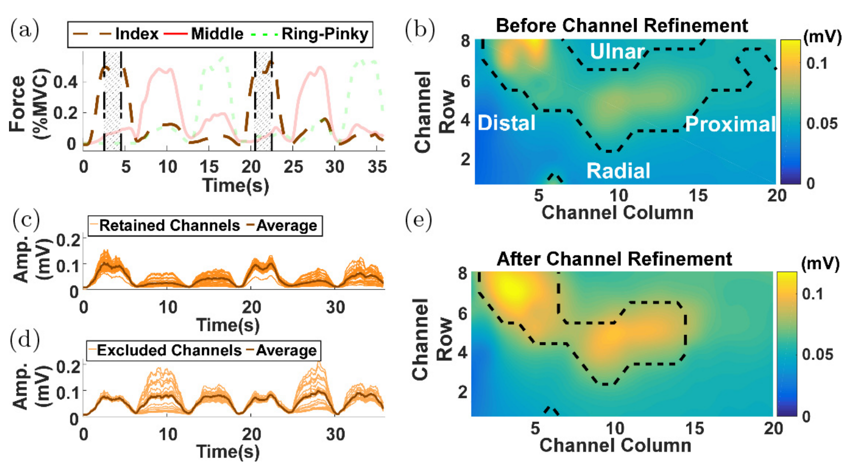

Fig. 3. Electromyogram (EMG) channel selection and refinement procedure of the EMG amplitude-based method. (a) The finger forces of the multi-finger trial used to perform the EMG channel refinement procedure. (b) The EMG distribution of a representative single-finger trial (same as shown in Fig. 2(a)) for the index finger. The dash lines encircle the 60 channels with the maximum EMG amplitude. (c) The EMG amplitudes of the retained channels have a stronger correlation (R^2 value) with the forces of the index finger, compared with the other two fingers. (d) The EMG amplitudes of the excluded channels after the refinement procedure have a weaker correlation with the forces of the index finger, compared with the other two fingers. (e) The EMG amplitude distribution when the index finger extended during the multi-finger trial. The index finger extension period was marked within the corresponding shaded period shown in (a). The dash lines encircle the retained EMG channels after the refinement procedure, which are used in the EMG-amp method.

(3) Select the 60 channels with the largest amplitude for individual fingers, obtaining the EMG channel pool $\mathrm{C}_{60,\mathrm{I}}$, $\mathrm{C}_{60,\mathrm{M}}$, and $\mathrm{C}_{60,\mathrm{RP}}$ (Fig. 3(b)). The channel number of 60 was selected based on our initial test such that most EMG activities can be captured.
(4) For a given multi-finger trial in the testing set, calculate the EMG amplitude of individual channels in the EMG channel pools using the sliding window, and then average across the channels within individual channel pools, resulting in the time courses of overall EMG amplitude for individual fingers, i.e. $\mathbf{A}_{60,l}$, $l = \mathrm{I}, \mathrm{M}, \mathrm{RP}$.
(5) Smooth the $\mathbf{A}_{60,l}$ using the Kalman filter.
(6) Process the force of individual fingers using the sliding window, resulting in $\mathbf{F}_l^{\mathrm{tst}}(l = \mathrm{I}, \mathrm{M}, \mathrm{RP})$.
(7) Use a linear regression model to predict the force level of individual fingers

$$\mathbf{F}_l^{\mathrm{tst}} = c_l \mathbf{A}_{60,l} + d_l \quad l = \mathrm{I}, \mathrm{M}, \mathrm{RP}, \tag{6}$$

and the resultant R^2 value and RMSE were used to evaluate the force prediction performance.

As a preliminary selection of EMG channels for individual fingers, there is a substantial overlap of EMG channels between fingers,[54] as shown in Fig. 3(b), cross-talk related interference of the EMG amplitude may bias the force prediction. In addition, different fingers have muscle compartments with different spatial distributions, a fixed channel number can also bias the EMG amplitude. Therefore, a second EMG amplitude-based method was performed, which further refined the EMG channel pool to reduce EMG channel overlap (termed the EMG-amp method). The major difference compared with the EMG60-amp method was that a channel refinement procedure was added after Step (3) of the EMG60-amp method. The specific channel refinement procedures are described as follows:

(1) For a given multi-finger trial in the training set, calculate the time courses of EMG amplitude of individual channels in the EMG channel pool $\mathrm{C}_{60,\mathrm{I}}$, $\mathrm{C}_{60,\mathrm{M}}$, and $\mathrm{C}_{60,\mathrm{RP}}$ using the sliding window, obtaining $\mathbf{p}_{i,\mathrm{I}}$, $\mathbf{p}_{j,\mathrm{M}}$, and $\mathbf{p}_{k,\mathrm{RP}}$ $(i, j, k = 1, 2, \ldots, 60)$.
(2) Process the force data using the sliding window, resulting in time courses of force $\mathbf{F}_l^{\mathrm{trn}}(l = \mathrm{I}, \mathrm{M}, \mathrm{RP})$.
(3) Perform a linear regression analysis between individual EMG amplitudes $\mathbf{p}_{i,l}$ and individual forces $\mathbf{F}_l^{\mathrm{trn}}$, obtaining the coefficient of determination R^2_{i,l_1-l_2} between the ith channel in the channel pool C_{60,l_1} and the force of finger l_2 $(i = 1, 2, \ldots, 60,\ l_1, l_2 = \mathrm{I}, \mathrm{M}, \mathrm{RP})$.
(4) If $R^2_{i,l_1-l_1} < R^2_{i,l_1-l_2}$ and $l_2 \neq l_1$, then remove the ith channel from the channel pool C_{60,l_1}, resulting in the refined channel pool for individual fingers, i.e. C_I, C_M, and C_RP, which can be used for force prediction in the EMG-amp method.

For example, Fig. 3(a) illustrates the forces of a multi-finger trial used to refine EMG channels. Figure 3(c) illustrates the EMG amplitudes of the retained channels that had a stronger correlation (R^2 value) with the force level of the index finger compared with other fingers (middle and RP). Figure 3(d) shows the channels excluded from the 60-channel pool since their amplitudes had a stronger correlation with other finger forces. The refined EMG channels are shown as the encircled area in Fig. 3(e) for the index finger.

2.4. *Detection of muscle contraction state*

Both the recorded forces and the predicted forces using different methods were further categorized into two states, i.e. active and rest, in order to investigate the performance of different methods on identifying the muscle contraction or relaxation states. Specifically, the recorded and predicted forces were averaged separately within each plateau of the targeted force trace for individual fingers. If the force was above a threshold (2%, 5%, or 10% MVC), it was considered an active state. Otherwise, it was considered a rest state. The states calculated based on the actual forces were considered the true states. The states identified from the predicted forces were compared with the true states, and three metrics were evaluated: the false active rate, false rest rate, and the accuracy. The false active rate was defined as the number of the rest cases that were falsely identified as active normalized by the total number of true rest cases. The false rest rate was defined as the number of the active cases that were falsely identified as rest normalized by the total number of true active cases. The accuracy was calculated as the number of

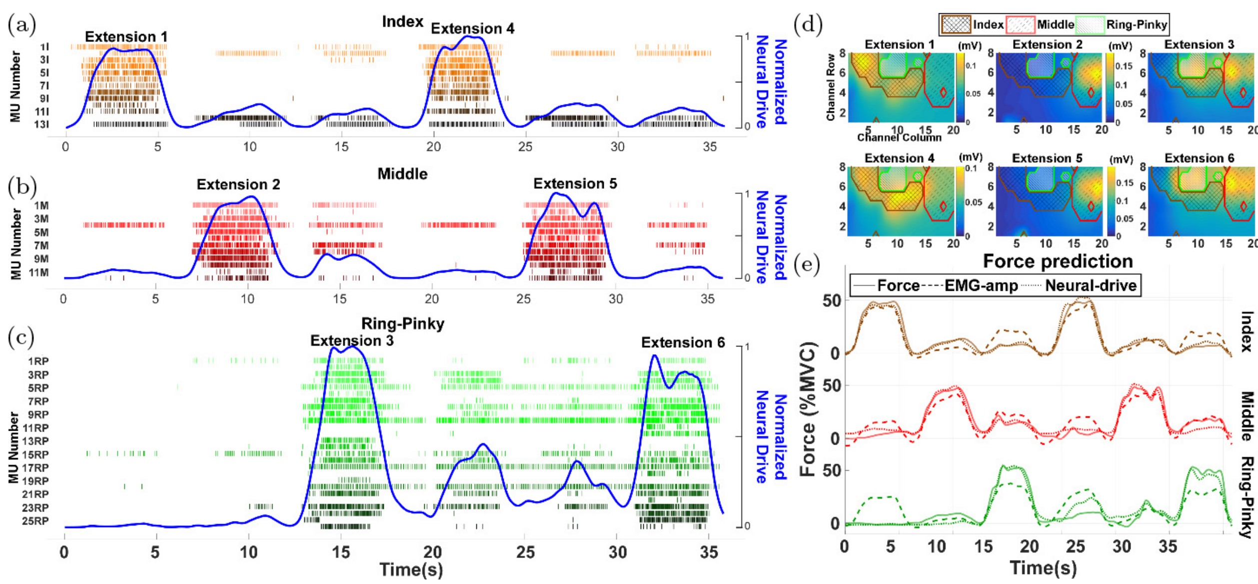

Fig. 4. (Color online) A representative example of concurrent and continuous force prediction of different fingers. (a)–(c) The firing event trains of MUs of the index, middle, and ring-pinky (RP) fingers are shown. The overlaid blue curves show the normalized populational discharge frequency of individual fingers. (d) The EMG amplitude distribution for the six repetitions when the force of a specific finger is plateaued. The solid lines encircle the EMG channels used to predict the overall EMG amplitude for individual fingers in the EMG-amp method. (e) The force prediction of the neural-drive method and the EMG-amp method is shown.

correctly identified active and rest cases normalized by the total number of cases.

3. Results

3.1. *Force prediction performance*

3.1.1. *Force prediction results of a representative trial*

Figures 4(a)–4(c) illustrate the MU firing event trains used to predict forces of the index, middle, and RP fingers, respectively from a representative multi-finger trial in the testing set. The populational firing frequency (blue curves) of all the MUs was calculated to represent the strength of the neural drive for individual fingers. Figure 4(d) displays the EMG amplitude distribution when the force of the specific fingers reached the target, and the EMG channels used for individual fingers in the EMG-amp method. The trial contained six repetitions of extensions as shown in Fig. 4(e). A linear regression was performed between the neural-drive signals of individual fingers and the corresponding finger forces, as well as between the overall EMG amplitude of individual fingers and the corresponding finger forces. The force prediction results based on the regression analysis are shown in Fig. 4(e). The predicted force using the neural-drive method followed the actual force accurately. In contrast, overestimation and underestimation errors were evident using the EMG-amp method.

3.1.2. *Performance measured with R^2 and RMSE*

To evaluate whether the neural-drive method can improve force prediction performance across subjects, their performances were compared using the R^2 value and the RMSE. The R^2 value (Fig. 5(a)) and the RMSE (Fig. 5(b)) were first averaged across trials and then averaged across fingers to compare the overall force prediction performance. The repeated measures analysis of variance (ANOVA) demonstrated that three force prediction methods (neural-drive, EMG-amp, and EMG60-amp) showed significant differences in both the R^2 value ($F(2, 14) = 22.12$, $p < 0.0001$, where 2 is the DOF of the method, 14 is the DOF of error) and the RMSE ($F(2, 14) = 17.36, p = 0.0002$). Further *post-hoc* test with Holm–Bonferroni correction showed that the R^2 value of the neural-drive method was significantly larger than those of both EMG amplitude-based

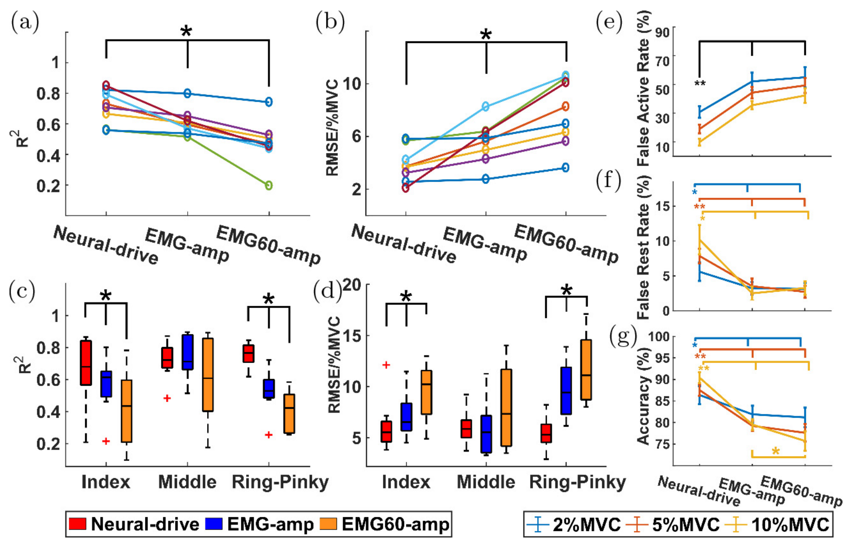

Fig. 5. (a) The average correlation (R^2 value) between the predicted and actual forces for individual subjects, (b) the average root-mean-square-error (RMSE) between the predicted and actual forces for individual subjects, (c) the average R^2 value of individual fingers, (d) the average RMSE of individual fingers, (e) the average false active rate across all subjects, (f) the average false rest rate across all subjects, and (g) the average accuracy across all subjects. The error bars represent the standard error. $^*p < 0.05$, $^{**}p < 0.01$.

methods ($p < 0.05$), and the R^2 value of the EMG-amp method was significantly larger compared with the EMG60-amp method ($p < 0.05$). The comparison of the RMSE also demonstrated that the RMSE of the neural-drive method was significantly smaller compared with both EMG amplitude-based methods ($p < 0.05$). The RMSE of the EMG-amp method was also significantly smaller compared with the EMG60-amp method ($p < 0.05$).

To further evaluate the performance of the three methods for individual fingers, the R^2 value and the RMSE were averaged across trials for individual fingers as shown in Figs. 5(c) and 5(d). The repeated measures ANOVA showed that there were significant differences of the R^2 value and the RMSE between the three methods for both the index and the RP fingers ($p < 0.05$). However, there was no significant difference of either the R^2 value ($F(2, 14) = 2.05, p = 0.1653$) or the RMSE ($F(2, 14) = 2.12, p = 0.1572$) for the middle finger. Further *post-hoc* tests showed that the R^2 value of the neural-drive method was significantly larger than those of both EMG amplitude-based methods for both the index and RP fingers ($p < 0.05$), and the R^2 value of the EMG-amp method was also significantly larger than the EMG60-amp method for both the index and RP fingers ($p < 0.05$). As for the RMSE, the neural-drive and the EMG-amp methods had significantly smaller force prediction errors compared with the EMG60-amp method ($p < 0.05$) for the index finger. However, the improvement of the neural-drive method compared with the EMG-amp method was not significant ($p = 0.0743$). For the RP finger, the RMSE of the neural-drive method was significantly smaller compared with the other two EMG amplitude-based methods ($p < 0.05$), and the EMG-amp method also had a significantly smaller RMSE value compared with the EMG60-amp method ($p < 0.05$).

3.1.3. *Performance measured with detection accuracy of muscle contraction state*

Finally, the number of false detections of finger activations was evaluated. Figures 5(e)–5(g) illustrate the average false active rate, false rest rate, and the accuracy across all subjects, respectively, when different thresholds were used. The repeated measures ANOVA showed that the false active rate differed significantly between the three methods (neural-drive, EMG-amp, and EMG60-amp) regardless the choice of the threshold (2% MVC: $F(2, 14) = 16.52$, $p = 0.0002$; 5% MVC: $F(2, 14) = 24.45$, $p < 0.0001$; 10% MVC: $F(2, 14) = 29.02$, $p < 0.0001$). Further

Table 1. Performance measurements.

	Neural-drive (mean ± S.D.)			EMG-amp (mean ± S.D.)			EMG60-amp (mean ± S.D.)		
$R2$[a]	0.71 ± 0.11			0.61 ± 0.09			0.48 ± 0.15		
RMSE/%MVC[a]	5.88 ± 1.34			7.56 ± 1.60			9.75 ± 2.55		
	Index	Middle	Ring-pinky	Index	Middle	Ring-pinky	Index	Middle	Ring-pinky
$R2$[b]	0.66 ± 0.22	0.72 ± 0.12	0.76 ± 0.08	0.57 ± 0.17	0.74 ± 0.14	0.53 ± 0.14	0.42 ± 0.25	0.60 ± 0.27	0.40 ± 0.13
RMSE/%MVC[b]	6.17 ± 2.62	6.02 ± 1.65	5.43 ± 1.61	7.15 ± 2.20	5.88 ± 2.69	9.66 ± 2.78	9.51 ± 2.77	7.99 ± 4.21	11.75 ± 3.50
	2% MVC	5% MVC	10% MVC	2% MVC	5% MVC	10% MVC	2% MVC	5% MVC	10% MVC
False active rate (%)	30.74 ± 11.36	18.93 ± 8.36	9.80 ± 6.54	52.09 ± 17.39	44.26 ± 11.51	35.49 ± 8.01	54.92 ± 20.14	49.26 ± 14.85	42.25 ± 14.72
False rest rate (%)	5.60 ± 3.75	7.86 ± 2.96	10.21 ± 5.95	3.22 ± 2.54	3.51 ± 3.15	2.50 ± 2.69	3.14 ± 2.42	2.72 ± 2.39	3.26 ± 2.80
Accuracy (%)	86.38 ± 5.92	87.52 ± 3.66	90.41 ± 3.55	81.90 ± 5.65	79.22 ± 3.45	79.51 ± 3.55	81.19 ± 6.40	77.62 ± 5.73	75.72 ± 6.36

Note: [a]The results averaged across trials and all fingers.
[b]The results averaged across trials for individual fingers, S.D., standard deviation.

post-hoc test showed that the false active rate of the neural-drive method was significantly smaller than both EMG amplitude-based methods ($p < 0.01$), while there was no significant difference between the EMG-amp method and the EMG60-amp method ($p > 0.05$). However, the false rest rate of the neural-drive method was higher than the other two methods. The repeated measures ANOVA results showed that there were significant differences between the three methods for all the thresholds (2% MVC: $F(2, 14) = 6.95$, $p = 0.008$; 5% MVC: $F(2, 14) = 27.96$, $p < 0.0001$; 10% MVC: $F(2, 14) = 11.96$, $p = 0.0009$). *Post-hoc* test showed that the false rest rate of the neural-drive method was significantly larger than both EMG amplitude-based methods (2% and 10% MVC: $p < 0.05$; 5% MVC: $p < 0.01$), and there was no significant difference between the two EMG amplitude-based methods for any of the three thresholds ($p > 0.05$). As for the overall accuracy, there were also significant differences between the three methods (2% MVC: $F(2, 14) = 8.51$, $p = 0.0038$; 5% MVC: $F(2, 14) = 15.65$, $p = 0.0003$; 10% MVC: $F(2, 14) = 18.47$, $p < 0.0001$). *Post-hoc* test showed that the neural-drive method obtained a significantly higher accuracy compared with the other two methods for all the thresholds (2% MVC: $p < 0.05$; 5% and 10% MVC: $p < 0.01$). Meanwhile, the accuracy of the EMG-amp method was significantly higher than the EMG60-amp method when 10% MVC was selected as the threshold ($p < 0.05$).

3.2. *Overlap of muscle activity distribution between fingers*

We further analyzed the relation between the amount of the muscle activity overlap and the force prediction error (RMSE). Figure 6(a) illustrates the peak-to-peak amplitude distribution of the MUAP from three representative MUs for the index, middle, and RP fingers, respectively. The MUAP of individual channels was obtained through a spike triggered averaging of the 8×20-channel EMG signals from the single-finger trials.[55] Figure 6(b) shows the average EMG amplitude distribution across all the

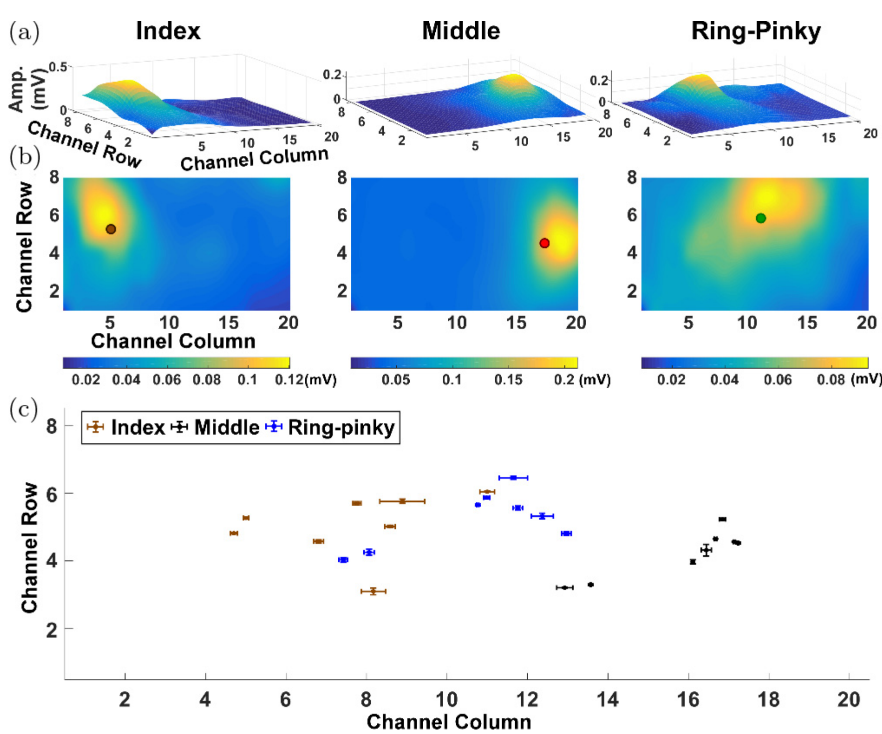

Fig. 6. Electromyogram (EMG) amplitude distribution analysis. (a) The motor unit action potential (MUAP) amplitude (monopolar peak-to-peak) distribution of three representative MUs for the index, middle, and ring-pinky (RP) fingers, respectively. (b) The EMG amplitude distribution across all single-finger trials for individual fingers from a representative subject. The dots represent the centroids of the amplitude distribution. (c) The average centroid positions across all single-finger trials for individual fingers and individual subjects.

corresponding single-finger trials. Figure 6(c) shows the average positions of the centroids from all the single-finger trials for individual subjects. The centroids of the index and RP fingers were close to each other but were relatively far from the centroid of the middle finger.

3.2.1. *Centroid distance of EMG distribution between fingers*

The distance between the centroids of any two fingers was then calculated for individual subjects. Figure 7(a) illustrates the range of the centroid distance from all subjects. The repeated measures ANOVA showed that there was significant difference between the three centroid distances i.e. the distance between index & middle fingers, the distance between index & RP fingers, and the distance between middle & RP fingers ($\text{F}(2, 14) = 17.12, p = 0.0002$). Further *post-hoc* test showed that the index & middle centroid distance was significantly larger than the index & RP distance ($p < 0.01$), and the middle & RP distance ($p < 0.05$). The middle & RP centroid distance was numerically larger than the index & RP centroid distance. However, the difference was not significant ($p = 0.0650$).

3.2.2. *2-D correlation coefficient of EMG distribution between fingers*

The 2-D correlation coefficient was used to further quantify the amount of overlap of EMG amplitude distribution between fingers. The EMG amplitude distribution was first averaged across all single-finger trials for individual fingers and then used to calculate the 2-D correlation coefficient between any two fingers. Figure 7(b) illustrates the range of the correlation coefficient between any two fingers from all subjects. The repeated measures ANOVA showed that there was a significant difference between the three types of overlap coefficients ($\text{F}(2, 14) = 7.87$, $p = 0.0051$). Further *post-hoc* test showed that the index & RP correlation coefficient was significantly larger than that between the index and middle fingers ($p < 0.01$), and that between the middle and RP fingers ($p < 0.05$).

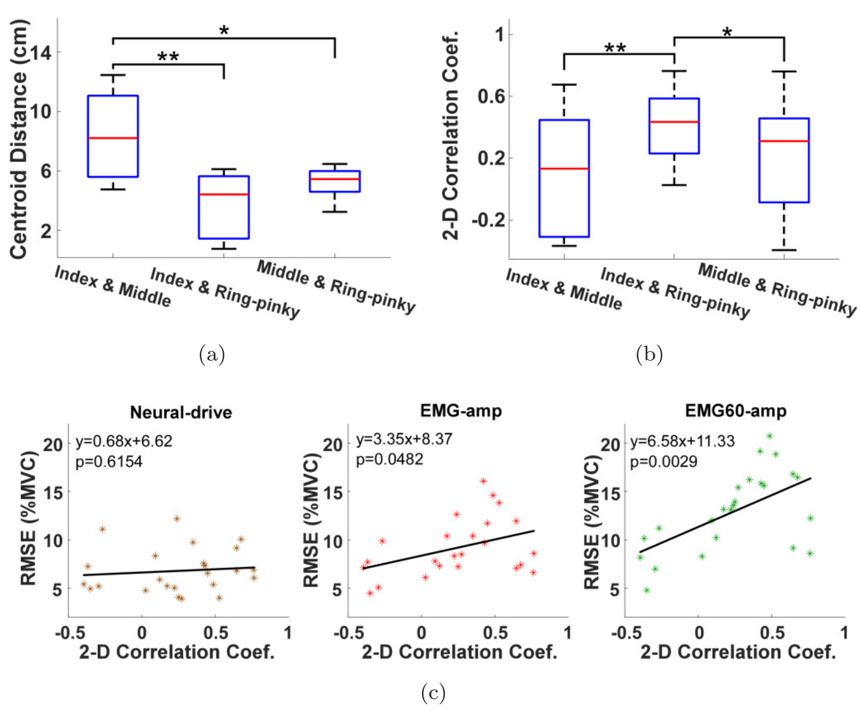

Fig. 7. (a) The range of the centroid distance between the index and middle fingers, between the index and ring-pinky (RP) fingers, and between the middle and RP fingers. (b) The range of the 2D correlation coefficient between the index and middle fingers, between the index and RP fingers, and between the middle and RP fingers. (c) Pearson correlation between the RMSE and the 2-D correlation coefficient of the three methods. $^{*}p < 0.05$, $^{**}p < 0.01$.

3.2.3. *Correlation between EMG distribution overlap and force prediction error*

In order to quantify the relation between the amount of muscle activity overlap and the force prediction error, the RMSE values were first calculated for each repetition when the target force reached the maximum, i.e. within the shaded period as determined by the dash lines in Fig. 3(a), for individual fingers. Then, the RMSE values of any two fingers were averaged across all extensions and all trials, which resulted in three RMSE values for each subject. Similarly, three 2-D correlation coefficients between fingers were also calculated for each subject. Then, all three RMSE values with their corresponding 2-D correlation coefficients were pooled together to perform the Pearson correlation analysis (Fig. 7(c)). The results showed that there was a significant correlation between the RMSE value and the 2-D correlation coefficient when the two EMG amplitude-based methods were used (EMG-amp: $r = 0.4073$, $p < 0.05$, EMG60-amp: $r = 0.5807$, $p < 0.01$). On the contrary, the RMSE was not influenced by the muscle activity overlap when the neural-drive method was used ($r = 0.1080$, $p > 0.05$).

4. Discussion

This study sought to concurrently and continuously predict dexterous isometric extension forces of individual fingers based on source separation of MU pool discharge information. We decomposed the EMG signals to obtain the information of MUs. The MUs were then classified into different groups specific to individual fingers. The populational firing frequency of MUs were used to predict extension forces of individual fingers. The results demonstrated that the neural-drive method based on MU firing activities had a significantly better force prediction performance (a higher R^2, a lower RMSE, and a high accuracy of detecting finger active or rest states) compared with the conventional EMG amplitude-based methods. Compared with the global EMG-based force prediction methods, these findings indicate that the MU pool binary firing events are more robust for concurrent and continuous force predictions of individual fingers. The outcomes can help provide a robust neural-machine interface that can allow users to intuitively control advanced robotic hands in a dexterous manner.

The improved performance of the neural-drive method compared with the EMG-amp method largely arose from several aspects. Certain channels still contained cross-talk of different fingers due to proximity of finger muscle compartments,[54,56] which resulted in overestimated and underestimated forces. When the muscles of different fingers are anatomically close to each other, it is inevitable for an electrode to capture the activities of other muscles. In contrast, the key procedure to classify the MUs specific to individual fingers made it possible to predict the neural drive signals of individual fingers concurrently and independently, thereby resulting in more accurate force predictions of individual fingers, even when muscles are anatomically close to each other.

This can also be demonstrated by the correlation analysis between the force prediction errors and the muscle activity overlap, and the performance of detecting muscle states. The correlation analysis showed that the amount of muscle activity overlap between fingers can significantly influence the performance of both EMG amplitude-based methods, but no significant influence was observed on the prediction error using the neural-drive method. The false active rate of both EMG amplitude-based methods was significantly higher compared with the neural-drive method, mainly due to the markedly reduced force overestimation in the neural-drive method. In addition, compared with the EMG amplitude information, the binary firing events were less influenced by various sources of interference to the EMG recordings, such as cancellation of MUAPs, variations of MUAP amplitude, background noise, and motion artifacts. For example, motion artifacts can lead to a significant increase of the estimated EMG amplitude and an overestimation of the finger force. On the contrary, a motion artifact can only lead to the false detection of one or several firing events, which have little influence on the estimation of the firing rate of the MU pool and the estimation of the finger force.

It has been demonstrated that the neural-drive method was more accurate compared with the EMG amplitude-based method for all fingers on either force prediction.[38] or joint kinematic prediction.[39] In these studies, the experiment was well controlled such that subjects were instructed to extend one finger at a time and any co-contraction was avoided. Finger forces or joint angles were predicted for one finger at a time. On the other hand, in this study, co-contractions were allowed, and the forces of different fingers were predicted concurrently. In our study, the performance of the neural-drive and the EMG-amp methods was comparable for the middle finger, partly because the muscle activation region of the middle finger was far away from that of the index and RP fingers,[54] resulting in a minimal cross-talk from the index and RP fingers. The inconsistency compared with the previous studies[38,39] could arise from two factors. First, there was no EMG channel refinement procedure in the previous studies, which improved the performance of the EMG amplitude-based method in the current study. Second, different from the previous study,[38] the separation vectors used to extract the MU firing event trains for neural-drive calculation in the multi-finger trials were obtained through the EMG decomposition information obtained from the single-finger trials. The variation of the MUAP shape between trials can arise from the shift of electrodes.[57] and muscle morphology change, which could lead to degradation of the accuracy of the firing events.[37] Even though the performance of the EMG amplitude-based method and the neural-drive method was comparable for the middle finger, we expect that the neural-drive method can outperform the EMG amplitude-based method with prolonged muscle contractions.[37]

The muscle contraction state was also simplified into two states, i.e. rest and active. For realistic applications, it was relevant to identify the muscle contraction state accurately for making decisions when to start and stop the actuators of robotic devices. Since the EMG amplitude-based method can fail to distinguish the force between different fingers, especially between the index and RP fingers, a number of rest states can be falsely identified as active states, resulting a higher false active rate. Surprisingly, the EMG-amp method after channel refinement showed no significant improvement in muscle contraction state detection, compared with the EMG60-amp method. This may be due to a substantial level of force overestimation above the selected thresholds, which can still lead to state detection errors. In contrast, the false active rate of the neural-drive method was significantly smaller than both EMG amplitude-based methods. The results indicated that the force overestimation was markedly reduced in the neural-drive method. The false rest rate using the neural-drive method, however, was significantly higher compared with the EMG amplitude-based methods, which indicated that the neural-drive method may fail to detect small force levels. The possible sources of error were that the small MUs recruited at low force levels were not identified in the MU pool of different fingers, because the MU information was obtained via decomposing EMG recordings from the trials with large contraction forces (50% MVC). Adding additional MU information decomposed from trials with low force levels may help to improve the ability of the neural-drive method to accurately predict low forces. In addition, the firing rate to MU force relation has a relatively shallow slope.[58] The sparse firing events at the low excitation drive may underestimate the muscle force, when a linear regression function is developed at moderate to high force levels. Even though the neural-drive method had a larger false rest rate, the overall accuracy of the neural-drive method was significantly higher compared with the EMG amplitude-based methods, demonstrating the high performance of the neural-drive method in identifying active muscle contraction states from rest states.

Although the results were promising in the prediction of individual finger forces,[38] the iteration procedure in the Fast-ICA algorithm was time consuming and infeasible for direct real-time applications. Instead of repeating the iterations for every trial to predict the muscle force, the separation vectors obtained using the single-finger trials were directly applied to the EMG data from the multi-finger trials in this study. Therefore, it is feasible to obtain the MU separation vector information during an initialization phase, and the MU firing information can then be obtained in real-time using the pre-computed separation vectors, which can be used to predict finger forces in real time. Even though the MUAP features can change over time, resulting in a degradation of the separation matrix to extract the discharge information of motoneurons, the detected firing events were still valid to predict the force accurately in the real-time condition, compared with the EMG amplitude-based method, especially with prolonged contractions.[37]

One limitation of this study was that the force prediction was performed during isometric contraction conditions. Previous studies have used motoneuron discharge information to predict finger joint movements.[39] Clearly, further studies are necessary to evaluate the performance of the neural-drive method during dynamic muscle contractions with multi-finger motions.

The other limitation is that the thumb was not involved in this study. A neural-machine interface for the realistic control of prosthetic hands should have the ability to decode the movement intention of the thumb, which plays an important role in daily life. The main contribution of this study is that the MU firing information was used to decode the isometric force of individual fingers concurrently by classifying the MUs associated with different fingers. The proposed method alleviated the cross-talking issue when different muscles are anatomically close to each other. Therefore, it is reasonable to speculate that the proposed method can also be applied to decode the thumb force. Its performance will be explored on the thumb in future studies.

This study can help in developing a reliable neural-machine interface for the control of external devices, such as the control of prosthetic hands for amputees or the control of remote devices for able-bodied individuals. In this study, we focused on the able-bodied individuals and the results are promising. In amputees, the available muscles can be different from able-bodied subjects, especially considering the varied level of amputation. Meanwhile, the inaccessibility of finger forces or kinematics also brings challenges to the classification of MUs. Therefore, in our further study, it is necessary to evaluate the performance of our method on amputees. In addition, only one female participant was recruited. Considering the relatively low EMG activity level in female participants, the number of detectable MUs and the accuracy of the firing events might be decreased, which might degrade the performance of the neural-drive method. However, the degraded EMG recordings could also decrease the performance of the EMG amplitude-based method. In our further study, we will explore whether the performance of the neural-drive method differs between male and female participants.

5. Conclusion

In summary, the goal of this study was to concurrently predict individual finger forces using MU firing information. The extracted firing information was used to reliably predict the finger forces even when the forces of different fingers varied in a dexterous manner. The developed key procedure to classify the MUs to be associated with different fingers was shown to be effective to alleviate the cross-talk issue of EMG recordings from multiple muscle compartments. This allowed the decoding of finger forces independently and concurrently. The findings can provide a robust neural-machine interface that could allow individuals with arm amputation to intuitively control wearable robotic hands or could allow trained individuals to remotely operate advanced robotic hands.

References

1. B. N. Perry, C. W. Moran, R. S. Armiger, P. F. Pasquina, J. W. Vandersea and J. W. Tsao, Initial clinical evaluation of the modular prosthetic limb, *Front. Neurol.* **9** (2018) 153.
2. A. Ortiz-Rosario, H. Adeli and J. A. Buford, Wavelet methodology to improve single unit isolation in primary motor cortex cells, *J. Neurosci. Methods* **246** (2015) 106–118.
3. A. Burns, H. Adeli and J. A. Buford, Brain–computer interface after nervous system injury, *Neuroscientist* **20** (2014) 639–651.
4. Q. Wu, Y. Zhang, J. Liu, J. Sun, A. Cichocki and F. Gao, Regularized group sparse discriminant analysis for p300-based brain-computer interface, *Int. J. Neural Syst.* **29** (2019) 1950002.
5. G. Dhillon, T. Kruger, J. Sandhu and K. Horch, Effects of short-term training on sensory and motor function in severed nerves of long-term human amputees, *J. Neurophysiol.* **93** (2005) 2625–2633.
6. A. Ortiz-Rosario, I. Berrios-Torres, H. Adeli and J. A. Buford, Combined corticospinal and reticulospinal effects on upper limb muscles, *Neurosci. Lett.* **561** (2014) 30–34.
7. A. Suberbiola, E. Zulueta, J. M. Lopez-Guede, I. Etxeberria-Agiriano and M. Grana, Arm orthosis/prosthesis movement control based on surface EMG signal extraction, *Int. J. Neural Syst.* **25** (2015) 1550009.

8. T. Lenzi, S. M. De Rossi, N. Vitiello and M. C. Carrozza, Intention-based EMG control for powered exoskeletons, *IEEE Trans. Biomed. Eng.* **59** (2012) 2180–2190.
9. A. O. Andrade and C. I. Andrade, On the relationship between features extracted from EMG and force for constant and dynamic protocols, *Annu. Int. Conf. IEEE Eng. Med. Biol. Soc.* **2012** (2012) 3392–3395.
10. A. Ortiz-Rosario and H. Adeli, Brain-computer interface technologies: From signal to action, *Rev. Neurosci.* **24** (2013) 537–552.
11. J. A. Barios, S. Ezquerro, A. Bertomeu-Motos, M. Nann, F. J. Badesa, E. Fernandez, S. R. Soekadar and N. Garcia-Aracil, Synchronization of slow cortical rhythms during motor imagery-based brain–machine interface control, *Int. J. Neural Syst.* **29** (2019) 1850045.
12. M. C. Corsi, M. Chavez, D. Schwartz, L. Hugueville, A. N. Khambhati, D. S. Bassett and F. De Vico Fallani, Integrating EEG and MEG signals to improve motor imagery classification in brain-computer interface, *Int. J. Neural Syst.* **29** (2019) 1850014.
13. M. Grana, M. Aguilar-Moreno, J. De Lope Asiain, I. B. Araquistain and X. Garmendia, Improved activity recognition combining inertial motion sensors and electroencephalogram signals, *Int. J. Neural Syst.* **30** (2020) 2050053.
14. S. H. George, M. H. Rafiei, A. Borstad, H. Adeli and L. V. Gauthier, Gross motor ability predicts response to upper extremity rehabilitation in chronic stroke, *Behav. Brain Res.* **333** (2017) 314–322.
15. S. H. George, M. H. Rafiei, L. Gauthier, A. Borstad, J. A. Buford and H. Adeli, Computer-aided prediction of extent of motor recovery following constraint-induced movement therapy in chronic stroke, *Behav. Brain Res.* **329** (2017) 191–199.
16. M. H. Rafiei, K. M. Kelly, A. L. Borstad, H. Adeli and L. V. Gauthier, Predicting improved daily use of the more affected arm poststroke following constraint-induced movement therapy, *Phys. Ther.* **99** (2019) 1667–1678.
17. Z. Yang, M. H. Rafiei, A. Hall, C. Thomas, H. A. Midtlien, A. Hasselbach, H. Adeli and L. V. Gauthier, A novel methodology for extracting and evaluating therapeutic movements in game-based motion capture rehabilitation systems, *J. Med. Syst.* **42** (2018) 255.
18. G. Hotson, D. P. McMullen, M. S. Fifer, M. S. Johannes, K. D. Katyal, M. P. Para, R. Armiger, W. S. Anderson, N. V. Thakor and B. A. Wester, Individual finger control of a modular prosthetic limb using high-density electrocorticography in a human subject, *J. Neural Eng.* **13** (2016) 026017.
19. Q. Wei, S. Zhu, Y. Wang, X. Gao, H. Guo and X. Wu, A training data-driven canonical correlation analysis algorithm for designing spatial filters to enhance performance of SSVEP-based BCIs, *Int. J. Neural Syst.* **30** (2020) 2050020.
20. G. S. Dhillon and K. W. Horch, Direct neural sensory feedback and control of a prosthetic arm, *IEEE Trans. Neural Syst. Rehabil. Eng.* **13** (2005) 468–472.
21. Y. Liu, Y. Ning, S. Li, P. Zhou, W. Z. Rymer and Y. Zhang, Three-dimensional innervation zone imaging from multi-channel surface EMG recordings, *Int. J. Neural Syst.* **25** (2015) 1550024.
22. A. Fougner, Ø. Stavdahl, P. J. Kyberd, Y. G. Losier and P. A. Parker, Control of upper limb prostheses: Terminology and proportional myoelectric control — A review, *IEEE Trans. Neural Syst. Rehabil. Eng.* **20** (2012) 663–677.
23. D. Leonardis, M. Barsotti, C. Loconsole, M. Solazzi, M. Troncossi, C. Mazzotti, V. P. Castelli, C. Procopio, G. Lamola, C. Chisari, M. Bergamasco and A. Frisoli, An EMG-controlled robotic hand exoskeleton for bilateral rehabilitation, *IEEE Trans. Haptics* **8** (2015) 140–151.
24. Z. Li, B. Wang, F. Sun, C. Yang, Q. Xie and W. Zhang, sEMG-based joint force control for an upper-limb power-assist exoskeleton robot, *IEEE J. Biomed. Health Inform.* **18** (2014) 1043–1050.
25. Z. Lu, X. Chen, X. Zhang, K.-Y. Tong and P. Zhou, Real-time control of an exoskeleton hand robot with myoelectric pattern recognition, *Int. J. Neural Syst.* **27** (2017) 1750009.
26. A. A. Adewuyi, L. J. Hargrove and T. A. Kuiken, An analysis of intrinsic and extrinsic hand muscle EMG for improved pattern recognition control, *IEEE Trans. Neural Syst. Rehabil. Eng.* **24** (2015) 485–494.
27. J. G. Ngeo, T. Tamei and T. Shibata, Continuous and simultaneous estimation of finger kinematics using inputs from an EMG-to-muscle activation model, *J. Neuroeng. Rehabil.* **11** (2014) 122.
28. J. N. Leijnse, N. H. Campbell-Kyureghyan, D. Spektor and P. M. Quesada, Assessment of individual finger muscle activity in the extensor digitorum communis by surface EMG, *J. Neurophysiol.* **100** (2008) 3225–3235.
29. J. Leijnse, S. Carter, A. Gupta and S. Mccabe, Anatomic basis for individuated surface EMG and homogeneous electrostimulation with neuroprostheses of the extensor digitorum communis, *J. Neurophysiol.* **100** (2008) 64–75.
30. T. Moritani, M. Muro and A. Nagata, Intramuscular and surface electromyogram changes during muscle fatigue, *J. Appl. Physiol.* **60** (1986) 1179–1185.
31. Y. Zheng and X. Hu, Dexterous force estimation during finger flexion and extension using motor unit discharge information, *Annu. Int. Conf. IEEE Eng. Med. Biol. Soc.* **2020** (2020) 3130–3133.
32. A. Gijsberts, R. Bohra, D. Sierra González, A. Werner, M. Nowak, B. Caputo, M. A. Roa and C. Castellini, Stable myoelectric control of a hand

prosthesis using non-linear incremental learning, *Front. Neurorobotics* **8** (2014) 8.

33. F. Xu, Y. Zheng and X. Hu, Real-time finger force prediction via parallel convolutional neural networks: A preliminary study, *Annu. Int. Conf. IEEE Eng. Med. Biol. Soc.* **2020** (2020) 3126–3129.
34. N. Nazmi, M. Abdul Rahman, S.-I. Yamamoto, S. Ahmad, H. Zamzuri and S. Mazlan, A review of classification techniques of EMG signals during isotonic and isometric contractions, *Sensors* **16** (2016) 1304.
35. D. Farina, I. Vujaklija, M. Sartori, T. Kapelner, F. Negro, N. Jiang, K. Bergmeister, A. Andalib, J. Principe and O. C. Aszmann, Man/machine interface based on the discharge timings of spinal motor neurons after targeted muscle reinnervation, *Nat. Biomed. Eng.* **1** (2017) 0025.
36. C. Heckman and R. M. Enoka, Physiology of the motor neuron and the motor unit, in *Handbook of Clinical Neurophysiology* (Elsevier, 2004), pp. 119–147.
37. Y. Zheng and X. Hu, Real-time isometric finger extension force estimation based on motor unit discharge information, *J. Neural Eng.* **16** (2019) 066006.
38. C. Dai, Y. Cao and X. Hu, Prediction of individual finger forces based on decoded motoneuron activities, *Ann. Biomed. Eng.* **47** (2019) 1357–1368.
39. C. Dai and X. Hu, Finger joint angle estimation based on motoneuron discharge activities, *IEEE J. Biomed. Health Inform.* **24** (2020) 760–767.
40. C. Dai, Y. Cao and X. Hu, Estimation of finger joint angle based on neural drive extracted from high-density electromyography, *Annu. Int. Conf. IEEE Eng. Med. Biol. Soc.* **2018** (2018) 4820–4823.
41. W. S. Yu, H. van Duinen and S. C. Gandevia, Limits to the control of the human thumb and fingers in flexion and extension, *J. Neurophysiol.* **103** (2009) 278–289.
42. C. E. Lang and M. H. Schieber, Human finger independence: Limitations due to passive mechanical coupling versus active neuromuscular control, *J. Neurophysiol.* **92** (2004) 2802–2810.
43. X. Hu, N. L. Suresh, C. Xue and W. Z. Rymer, Extracting extensor digitorum communis activation patterns using high-density surface electromyography, *Front. Physiol.* **6** (2015) 279.
44. Y. Zheng and X. Hu, Interference removal from electromyography based on independent component analysis, *IEEE Trans. Neural Syst. Rehabil. Eng.* **27** (2019) 887–894.
45. C. Dai and X. Hu, Independent component analysis based algorithms for high-density electromyogram decomposition: Experimental evaluation of upper extremity muscles, *Comput. Biol. Med.* **108** (2019) 42–48.
46. C. Dai and X. Hu, Independent component analysis based algorithms for high-density electromyogram decomposition: Systematic evaluation through simulation, *Comput. Biol. Med.* **109** (2019) 171–181.
47. A. Hyvärinen and E. Oja, Independent component analysis: Algorithms and applications, *Neural Netw.* **13** (2000) 411–430.
48. M. Chen, X. Zhang, Z. Lu, X. Li and P. Zhou, Two-source validation of progressive FastICA peel-off for automatic surface EMG decomposition in human first dorsal interosseous muscle, *Int. J. Neural Syst.* (2018).
49. F. Negro, S. Muceli, A. M. Castronovo, A. Holobar and D. Farina, Multi-channel intramuscular and surface EMG decomposition by convolutive blind source separation, *J. Neural Eng.* **13** (2016) 026027.
50. M. Chen and P. Zhou, A novel framework based on FastICA for high density surface EMG decomposition, *IEEE Trans. Neural Syst. Rehabil. Eng.* **24** (2016) 117–127.
51. D. Arthur and S. Vassilvitskii, *k-Means++: The Advantages of Careful Seeding* (Stanford, 2006).
52. Y. Zheng, G. Wang and J. Wang, Is using threshold-crossing method and single type of features sufficient to achieve realistic application of seizure prediction? *Clin. EEG Neurosci.* **47** (2016) 305–316.
53. E. A. Clancy and N. Hogan, Probability density of the surface electromyogram and its relation to amplitude detectors, *IEEE Trans. Biomed. Eng.* **46** (1999) 730–739.
54. X. Hu, N. L. Suresh, C. Xue and W. Z. Rymer, Extracting extensor digitorum communis activation patterns using high-density surface electromyography, *Front. Physiol.* **6** (2015) 279.
55. X. Hu, W. Z. Rymer and N. L. Suresh, Motor unit pool organization examined via spike-triggered averaging of the surface electromyogram, *J. Neurophysiol.* **110** (2012) 1205–1220.
56. C. Dai and X. Hu, Extracting and classifying spatial muscle activation patterns in forearm flexor muscles using high-density electromyogram recordings, *Int. J. Neural Syst.* **29** (2019) 1850025.
57. I. Rodríguez-Carreño, L. Gila-Useros and A. Malanda-Trigueros, Motor unit action potential duration: Measurement and significance, in *Advances in Clinical Neurophysiology* (InTech, 2012).
58. A. J. Fuglevand, D. A. Winter and A. E. Patla, Models of recruitment and rate coding organization in motor-unit pools, *J. Neurophysiol.* **70** (1993) 2470–2488.